CHEMISTRY OF MATERIALS

pubs.acs.org/cm

Article

Isotype Heterojunction Solar Cells Using n-Type Sb_2Se_3 Thin Films

Theodore D. C. Hobson, Laurie J. Phillips, Oliver S. Hutter, Huw Shiel, Jack E. N. Swallow, Christopher N. Savory, Pabitra K. Nayak, Silvia Mariotti, Bhaskar Das, Leon Bowen, Leanne A. H. Jones, Thomas J. Featherstone, Matthew J. Smiles, Mark A. Farnworth, Guillaume Zoppi, Pardeep K. Thakur, Tien-Lin Lee, Henry J. Snaith, Chris Leighton, David O. Scanlon, Vinod R. Dhanak, Ken Durose, Tim D. Veal, and Jonathan D. Major*

Cite This: *Chem. Mater.* 2020, 32, 2621−2630

Read Online

ACCESS | Metrics & More | Article Recommendations | Supporting Information

ABSTRACT: The carrier-type of the emerging photovoltaic Sb_2Se_3 was evaluated for both thin films and bulk crystals via a range of complementary techniques. X-ray photoelectron spectroscopy (XPS), hot probe, Hall effect, and surface photovoltage spectroscopy showed films and crystals synthesized from the Sb_2Se_3 granulate material to be n-type with chlorine identified as an unintentional n-type dopant via secondary ion mass spectrometry analysis. The validity of chlorine as a dopant was confirmed by the synthesis of intrinsic crystals from metallic precursors and subsequent deliberate n-type doping by the addition of $MgCl_2$. Chlorine was also shown to be a substitutional n-type shallow dopant by density functional theory calculations. TiO_2/Sb_2Se_3 n−n isotype heterojunction solar cells with 7.3% efficiency are subsequently demonstrated, with band alignment analyzed via XPS.

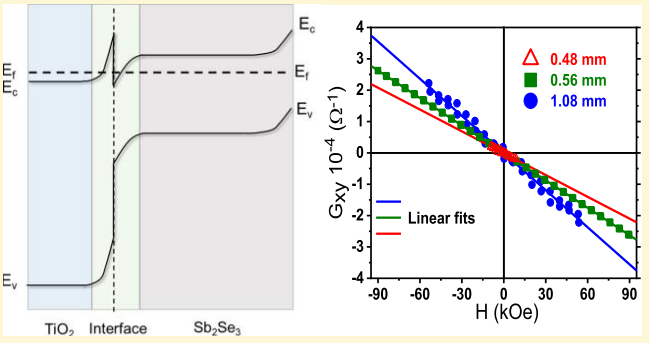

INTRODUCTION

Antimony selenide (Sb_2Se_3) solar cells are a comparatively recent addition to the thin-film photovoltaics family. Sb_2Se_3 has numerous selling points as a photovoltage (PV) material: it has high optical absorption of $>10^5$ cm^{-1}, a 1.18 eV direct bandgap,[1] contains no scarce or high-toxicity elements such as In, Te, Cd, or Pb, is a simple binary material minimizing secondary phase concerns, and has a nanoribbon grain structure,[2] suggesting that isotropic charge transport should be realizable and the recombination rates of grain boundaries should be greatly reduced.[3] Although a seemingly obvious candidate as a PV material, the first thin-film device efficiency of note was not reported until as recently as 2009 by Messina et al., who utilized a solution deposition process to achieve 0.66% power conversion efficiency (PCE).[4] It was not until the work of the Tang group, demonstrating ∼2% efficiency in early 2014 by either thermal evaporation[5] or a hydrazine-based solution process,[6] that interest in the technology started to increase. The field has rapidly developed since, primarily through vapor transport deposition techniques for Sb_2Se_3 and an indium tin oxide (ITO)/CdS/Sb_2Se_3 device structure to achieve PCE of 5.6% in 2015, 6.5% in 2017,[7] 7.5% in 2018,[8] and 9.2% in early 2019.[9] This rapid growth in efficiency means that Sb_2Se_3 has already exceeded the performance levels of long studied binary inorganics of high potential such as FeS_2 and SnS.[10,11] Research at the University of Liverpool has focused on the use of the well-established CdTe deposition technique of close space sublimation (CSS)[12−14] to develop a cell platform, which produces a material with preferable orientations compared to thermal evaporation routes, i.e., nanoribbons oriented perpendicular to the interface.[2] The use of CSS necessitated the development of an alternative SnO_2:F/TiO_2/Sb_2Se_3 device structure due to excessive interdiffusion with CdS, but yields carrier concentrations $>10^{17}$ cm^{-3}[2] and PCEs of over 6.6%[15] with open-circuit voltages (V_{oc}) beyond the current state of the art. Given the rapid growth of performance, this technology should easily exceed 10% PCE in the near future. Key to achieving this goal however will be development of a comprehensive understanding of the Sb_2Se_3 material, to align with the encouraging early stages of cell development.

A key assumption that has been made in the emergence of Sb_2Se_3 solar cells is that the absorber is predominantly p-type. Inorganic thin-film solar cells almost universally utilize p-type absorbers, with the exception of BiS_2.[1616] The majority of

Received: January 17, 2020
Revised: March 2, 2020
Published: March 3, 2020

reported Sb_2Se_3 devices also adopt the TCO/CdS/Sb_2Se_3 structure, common to CZTS, CIGS, and CdTe,[14] again all of which are p-type absorbers. The natural assumption is therefore that we have simply incorporated Sb_2Se_3 as an alternative p-type absorber into the existing device architecture. However, the actual carrier-type of Sb_2Se_3 is somewhat unclear and is often assumed to be p-type rather than measured. Work on high-purity single crystals showed the material to be insulating,[17] something supported by recent density functional theory (DFT) calculations,[18] which suggested significant midgap pinning due to native defects.

There are some reports of carrier-type determination in the solar cell material, although the results are typically from a single group and often inconclusive. Liu et al.[5] report Seebeck analysis showing the p-type character of thermally evaporated thin films, but subsequently draw the band structure based on X-ray photoelectron spectroscopy (XPS) analysis with a near insulating Fermi level. Zhou et al.[19] found p-type conductivity via cyclic voltammetry and Hall measurements, although Hall effect data were not shown. The same group has also latterly reported some n-type and insulating characters in devices. Zhou et al.[20] also suggested the formation of n-type Sb_2Se_3 regions near to the CdS interface due to Cd out-diffusion from the CdS layer, with the remainder of the Sb_2Se_3 layer being p-type. The mechanism by which Cd may act as an n-type donor is unclear, however. Recent work by the same group has further suggested Sb_2Se_3 to be insulating and a CdS/Sb_2Se_3/CuSCN device to function as an n−i−p structure.[21] How the insulating character of the material was determined was not specified.

In this paper, we conclusively demonstrate the n-type character of both single crystals and thin films of Sb_2Se_3 via a range of analysis techniques. We identify chlorine impurities as the source of the n-type doping and subsequently demonstrate $MgCl_2$ as an effective deliberate n-type dopant for single-crystal Sb_2Se_3. We thereby establish that the TCO/TiO_2/*n*-Sb_2Se_3/Au device structure produced is, in fact, an isotype n−n heterojunction device.

EXPERIMENTAL SECTION

Thin Film and Cell Fabrication. Sb_2Se_3 cells discussed in this work were deposited on the commercial SnO_2:F (fluorine-doped tin oxide (FTO))-coated soda-lime glass TEC10 from NSG Ltd. The device structure was glass/FTO/TiO_2/Sb_2Se_3/Au. TiO_2 layers were first deposited via radio frequency (RF) sputtering to a thickness of ∼10 nm at room temperature followed by a two-stage spin-coating process. A 250 μL concentration of 0.15 M titanium isopropoxide (TTIP) in ethanol solution was deposited on a 50 × 50 mm^2 substrate at 4000 rpm followed by 275 μL of 0.3 M TTIP in ethanol. The substrates were then air-annealed at 500 °C for 30 min. Sb_2Se_3 layers were deposited using the Alfa Aesar 5 N granulate material via CSS using a two-stage process.[15] First, a compact "seed" layer was deposited to ensure good coverage. This was done under vacuum at a source temperature of 350 °C with the substrate temperature being ramped from 250 to 390 °C over a period of 5 min. A second stage to deposit a larger grained film was then performed under 10 Torr of nitrogen at source and substrate temperatures of 460 and 410 °C, giving a film thickness of ∼1.5 μm. The Sb_2Se_3 source material is used for multiple (>100) depositions following an initial "bake" process performed at temperatures higher than used for growth to establish a consistent material baseline. No post-growth processing of the CSS material was employed. Gold back contacts (0.1 cm^2) were finally added via thermal evaporation.

Crystal Growth. Sb_2Se_3 single-crystal samples were grown using a vertical Bridgman melt-growth method. The crystal growth method was identical for all samples, with the only difference being in the source material used. For single crystals utilizing the nonintentionally doped Sb_2Se_3 (5 N purity Alfa Aesar), the source material granulate was used with no further additives. Undoped Sb_2Se_3 bulk crystals were synthesized from metallic Sb (6 N purity Alfa Aesar) and Se (5 N purity Alfa Aesar). In total, 8 g in total of metallic Sb and Se shot was added to a 16 mm diameter quartz tube. The elements were weighed to achieve a ratio close to stoichiometry, with a small (∼0.01 atom %) Se excess observed in the weighed elements. Ampoules were heated to 615 °C and then held for 24 h to allow full reaction and homogenization, before cooling to 300 °C at 1.5 °C/min. For $MgCl_2$-doped single crystals, 0.1 ± 0.02 atom % solid $MgCl_2$ was weighed, added to the undoped Sb_2Se_3 powder formed by the above process, and mixed. Sealed ampoules were lowered into a vertical single-zone furnace with the ampoule tip being held at the peak temperature point of 620 °C, set to be just above the 611 °C melting point of Sb_2Se_3.[22] A lowering rate of 1.15 mm/h through the furnace, for 7 days, with a temperature gradient of 6 °C/cm, was used. This produced crystals of 3 cm in length with the first 1.5−2 cm being large grained polycrystalline and the remaining section confirmed to be a single crystal. Further details are given in the paper by Hobson et al.[23]

Hot-Point Probe Technique. The hot-point probe was carried out using an in-house system. Samples were contacted with gold contacts, and gold point probes with a heat source were attached to one probe. The current generated was monitored via a Keithley 2400 source meter, as the current was found to produce more consistent data than the voltage for analysis of calibration samples.

Electronic Transport Measurements. For transport measurements, including Hall effect, square samples of ∼3 mm lateral size were cleaved from larger Sb_2Se_3 crystals doped with Cl. Thicknesses of the crystals used were in the 0.4−1 mm range. Indium contacts were soldered on the crystals in a van der Pauw geometry.[24] Four-terminal resistances were then measured DC using a Keithley 2400 source-measure unit in conjunction with a quantum design physical property measurement system (PPMS) (in perpendicular magnetic fields to 60 or 90 kOe) or a Janis Corporation flow cryostat in an electromagnet (to 10 kOe). All presented measurements were done at 300 K. Care was taken to select appropriate excitation currents to avoid non-Ohmic response and/or self-heating.

Surface Photovoltage Measurement (SPM). Surface photovoltage measurements (SPMs) were carried out using a vibrating Kelvin probe (KP) (probe diameter = 2 mm) (KP Technology, U.K.) to determine the surface work function (WF) in the dark and under illumination. All of the measurements were done in constant N_2 flow. To illuminate the whole surface, light from a 150 W quartz tungsten halogen lamp was incident on the sample using an optical fiber and lens at an angle of 45° with respect to the sample surface. This configuration allows illumination and probing from the same side.

The work function of the Kelvin probe was calibrated by a freshly cleaved highly ordered pyrolytic graphite surface.

Ultraviolet Photoemission Spectroscopy (UPS)/XPS/Hard X-ray Photoelectron Spectroscopy (HAXPES) Analysis. Ultraviolet photoemission spectroscopy (UPS) was performed using a He(I) discharge lamp in combination with a hemispherical electron-energy analyzer (PSP Vacuum Technology) with a 120 mm radius to detect photoelectrons, operated at a pass energy of 2 eV. X-ray photoemission spectroscopy (XPS) was performed using a SPECS monochromatic Al Kα ($h\nu$ = 1486.6 eV) X-ray source operated at 250 W and the same analyzer as for the UPS measurements using a pass energy of 10 eV. The narrower line width of the UPS source means that a better resolution is achieved with UPS over XPS. Hard X-ray photoelectron spectroscopy (HAXPES) was performed at the I09 beamline at the Diamond Light Source. A double-crystal Si(111) monochromator was used to select 5921 eV photons. A Si(004) channel-cut crystal was employed to monochromate the beam, improving the resolution. The end station is equipped with a VG Scienta EW4000 electron analyzer with ±30° angular acceptance. In all photoemission experiments performed, binding energies are stated with respect to the Fermi level, which was calibrated using the Fermi edge of a metal (cleaned polycrystalline silver or gold), also allowing the resolution of the systems to be determined (Δ_{UPS} = 0.13 eV, Δ_{XPS}

https://dx.doi.org/10.1021/acs.chemmater.0c00223
Chem. Mater. 2020, 32, 2621−2630

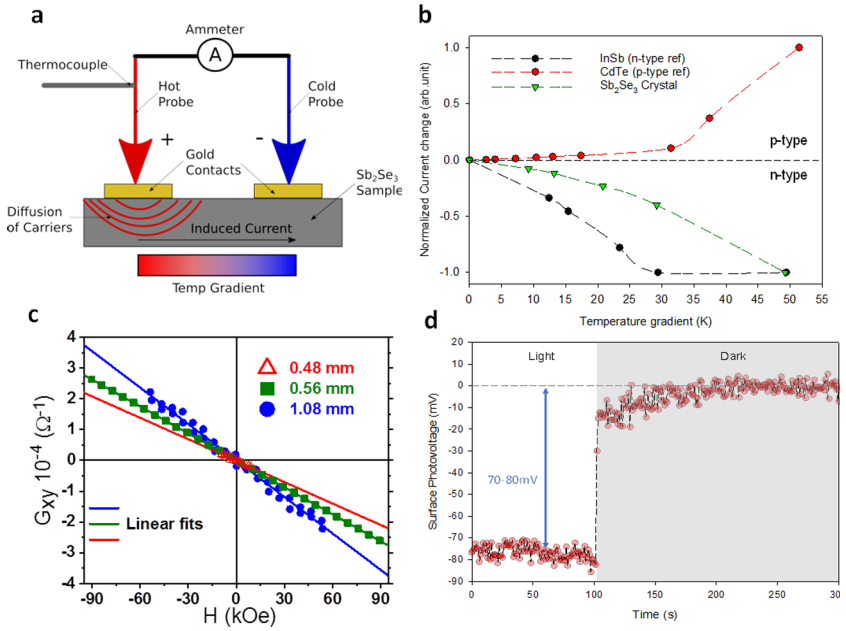

Figure 1. (a) Hot-probe measurement setup for bulk carrier-type determination, (b) normalized hot-probe data for the Sb_2Se_3 bulk crystal grown from the Sb_2Se_3 granulate with p-type and n-type reference crystals, (c) Hall conductance (G_{xy}) vs applied magnetic field (H) for three Sb_2Se_3 crystals with different thicknesses (0.48, 0.56, and 1.08 mm). The straight lines are linear fits to the corresponding data, which had zero field backgrounds subtracted and (d) surface photovoltage measurement of a TiO_2/Sb_2Se_3 device back surface.

= 0.43 eV, Δ_{HAXPES} = 0.28 eV). Bulk crystal samples were cleaved in situ to expose a clean surface, and all measurements were performed at room temperature. CSS thin films were measured using XPS and HAXPES without any in situ preparation.

Secondary Ion Mass Spectrometry (SIMS) Analysis. The time of flight secondary ion mass spectrometry (TOF-SIMS) of thin films was performed using an ION-TOF V instrument. The analysis beam was 25 keV Bi^{3+} with an analysis area of 50 μm square. The depth profiling beam was 1 keV Cs^+ operated with a raster size of 200 μm^2. To minimize the SIMS matrix effect, CsM+ cluster secondary ions were selected to obtain compositional depth profiles. Quadrupole SIMS of bulk crystals was performed using a Hiden Analytical gas ion gun and quadrupole detector. A beam of O^{2-} ions rastered over a 500 × 500 μm^2 area was used to sputter the sample using a beam energy of 5 keV at a current of 300 An.

DFT Calculations. Calculations were performed using density functional theory (DFT) within periodic boundary conditions using the Vienna Ab Initio Simulation Package (VASP).[25−28] The screened hybrid exchange-correlation functional HSE06 was used[29] for the electronic structure with geometry optimization of both bulk and defect supercells of Sb_2Se_3. Due to the layered nature of the Sb_2Se_3 structure, the D3 dispersion correction from Grimme et al. was also included in all calculations,[30] while spin−orbit coupling (SOC) was included for all bulk electronic structure calculations. Defect calculations were performed using the HSE06 + D3 method on a 1 × 3 × 1 supercell (60 atoms) with a Γ-centered 2 × 2 × 2 k-point mesh and a plane-wave energy cutoff of 350 eV. Spin−orbit coupling effects were not included in these calculations due to their expense and minimal structural effects; the relativistic renormalization at the k-points considered is also small (∼0.1 eV). To account for the "finite size effects" of the supercell and restore the dilute defect model, three corrections were used. First, a correction is necessary to ensure that the electrostatic potentials of the host and defect supercells are aligned.[31] Second, defects within supercells may interact with their own periodic images, causing the formation of a defect band; if this defect level is shallow, it may interact with a conduction or valence band, leading to erroneous filling with electrons and affecting the total energy. To counteract this, a "band filling" correction was applied.[32] Third, charged defects may interact with each other coulombically, due to the long-range behavior of such effects, and so a further "image charge" correction is required. In this report, we use the formalism of Murphy et al., as this accounts for anisotropy in the dielectric constant of the material, an effect that is strong for Sb_2Se_3.[33]

Device Characterization. Current−voltage (J−V) measurements were performed under AM1.5 illumination provided by a TS space system solar simulator. Capacitance voltage measurements were performed using a Solatron impedance analyzer. For external quantum efficiency (EQE) measurement, a Bentham PVE300 system was used

RESULTS

We were able to determine the carrier-type of bulk Sb_2Se_3 crystals grown from the granulate source material using a hot-probe technique,[34] shown schematically in Figure 1a. Two metal probes were contacted to a sample surface, with one probe being in contact with a heat source. The hot probe thermalizes carriers in the vicinity causing a diffusion current of free carriers, which can be read through an external ammeter. Depending on the majority carrier-type of the material, this produces either a positive or negative current gradient with temperature. The sign of the current gradient can thus be used to determine the carrier-type of unknown materials, for instance, when calibrated with reference to known n or p-type materials. This technique has the advantage of not requiring any specific sample preparation, being applicable even for relatively low doping densities and being a bulk measurement technique (i.e., it is independent of doping variations at the surface or contacting barriers[34]). Figure 1b shows hot-probe data recorded for both bulk crystal Sb_2Se_3, along with known compound semiconductor single-crystal reference samples of InSb (n-type) and CdTe (p-type). The current values were assessed over a ∼50 K range and have been normalized to allow easy comparison, as the magnitude of current recorded is highly sample-specific. The data show a negative gradient for Sb_2Se_3, indicating that it is n-type. This was confirmed by comparison to both reference samples,

https://dx.doi.org/10.1021/acs.chemmater.0c00223
Chem. Mater. 2020, 32, 2621−2630

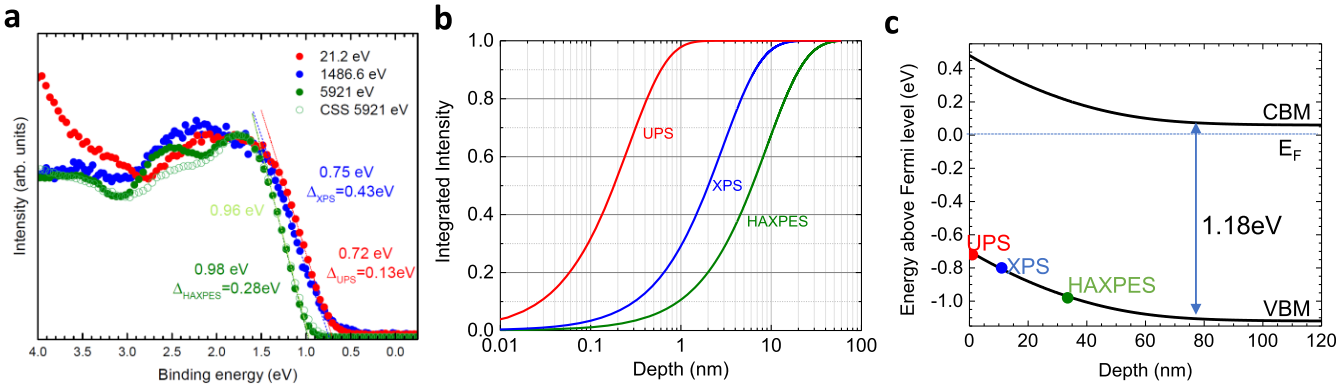

Figure 2. (a) Valence band spectra from a cleaved bulk crystal measured using HAXPES (5921.0 eV), XPS (1486.6 eV), and UPS (21.2 eV) with a CSS thin film measured by HAXPES for comparison (thin-film and crystal HAXPES data overlaps). Values are the VBM to Fermi level separation determined, with Δ values being the resolution of the technique; (b) integrated photoemission signal intensity as a function of depth for the three different photon energies used calculated using the TPP model of inelastic mean free paths; (c) determined band bending at the back surface from photoelectron measurements.

which showed the expected positive p-type and negative n-type gradients.

The majority carrier-type of the single-crystal material was also confirmed via Hall effect measurements. Figure 1c shows the 300 K Hall conductance (G_{xy}) vs applied magnetic field for three Sb_2Se_3 crystals of different thickness: 0.48, 0.56, and 1.08 mm. The Hall conductance G_{xy} is defined as $G_{xy} = \frac{R_{xy}}{R_s^2(0)}$ where R_{xy} is the Hall resistance and $R_s(0)$ is the sheet resistance at zero applied field. In all cases, simple linear behavior with a negative slope is found. Given the magnitude of the signal, the sizable mobility (see below), and the absence of nonlinearity to 90 kOe, we conclude a single dominant carrier-type, definitively electrons, i.e., n-type behavior. This is in accord with the results obtained from the hot probe in Figure 1a and other data discussed below, all of which indicate n-type carriers. The Hall coefficients, $R_H = -\frac{1}{|n|e}$, from the slopes of the straight-line fits in Figure 1c yield electron densities n of 3.99×10^{16}, 3.98×10^{16}, and 3.30×10^{16} cm^{-3} for the three crystals. The room-temperature resistivities (ρ) were 6.54, 5.46, and 6.04 Ω cm, giving carrier mobilities μ of 24.0, 28.7, and 31.3 $cm^2/(V\ s)$, respectively. The n, ρ, and μ values are thus in very reasonable agreement in these three crystals, the mobilities being easily large enough to rule out potential complications with nondiffusive transport.[35]

We note that thin-film layers produced by CSS from the Sb_2Se_3 granulate material were not able to be measured by either Hall effect or hot-probe measurements. The hot probe did not yield a sufficient signal to give a clear sign determination, while Hall measurements were frustrated by high resistivity, high contact resistance, and low apparent mobility. The measurement issues here may be a result of the material anisotropy and the necessity for the films to be deposited on an insulating substrate, i.e., glass. A large amount of prior work was required to optimize film orientation on FTO/TiO_2 for device applications.[2,15] The use of a glass substrate thus likely results in an unfavorable film orientation and low mobility in the plane of the measurement.[36]

Nevertheless, the n-type character of thin-film device layers was able to be confirmed by surface photovoltage measurement (SPV) using a Kelvin probe (KP). SPV measurements were carried out on the free back surface of a complete TiO_2/Sb_2Se_3 device structure, where the film orientation is optimized. SPV measurements show that the surface work function decreased under illumination (Figure 1d). This can be explained by the upward, i.e., from bulk to the surface, band bending, due to the trapping of electrons (the majority carrier of the semiconductor) on the surface. Upon illumination, the trapped electrons are screened by the photogenerated hole, which moves to the surface due to the band bending. This screening of electrons decreases the band bending, causing a decrease in surface work function. In this case, the effect is amplified due to the presence of the TiO_2 interface where the photogenerated holes encounter an energetic barrier. The SPV measurement thus identified n-type behavior of the thin-film Sb_2Se_3 material also, in agreement with the single-crystal measurements.

Further validation of the n-type character of the material was sought through a range of photoelectron spectroscopy techniques (UPS, XPS, and HAXPES), which were used to determine the work function at a range of penetration depths. Photoelectron spectroscopy work primarily focused on the single-crystal material as this provided a cleaner signal, and crystals could be in situ cleaved at the van der Waals bonds, removing the potential influence of surface oxide phases.[37] Confirmatory XPS and HAXPES analyses were also carried out on thin-film layers to check consistency with the crystal data.

Figure 2a shows photon energy-dependent photoemission of the valence band spectra of a cleaved bulk Sb_2Se_3 crystal for UPS, XPS, and HAXPES analyses with a CSS-grown thin-film HAXPES profile for comparison. The valence band maximum (VBM) to Fermi level separation is estimated by extrapolating the leading edge of the valence band photoemission to zero (Figure 2a). The higher the photon energy used, the higher the kinetic energy of the generated photoelectrons and the greater the effective probing depth, as illustrated in Figure 2b. The UPS spectrum probes the Fermi level and valence band position at ∼1 nm from the back surface compared to up to ∼30 nm for HAXPES. This depth-dependent photoemission allows not only determination of the doping-type via the Fermi level position but also an estimate of the band bending at the surface, as shown in Figure 2c. The Fermi level position in the bulk has been estimated using Hall-determined shallow doping levels (i.e., $\sim 10^{16}$–10^{17} cm^{-3}). For all depths probed, the Fermi level is always above the middle of the bandgap, demonstrating that the Sb_2Se_3 is n-type. This depth-dependent

https://dx.doi.org/10.1021/acs.chemmater.0c00223
Chem. Mater. 2020, 32, 2621−2630

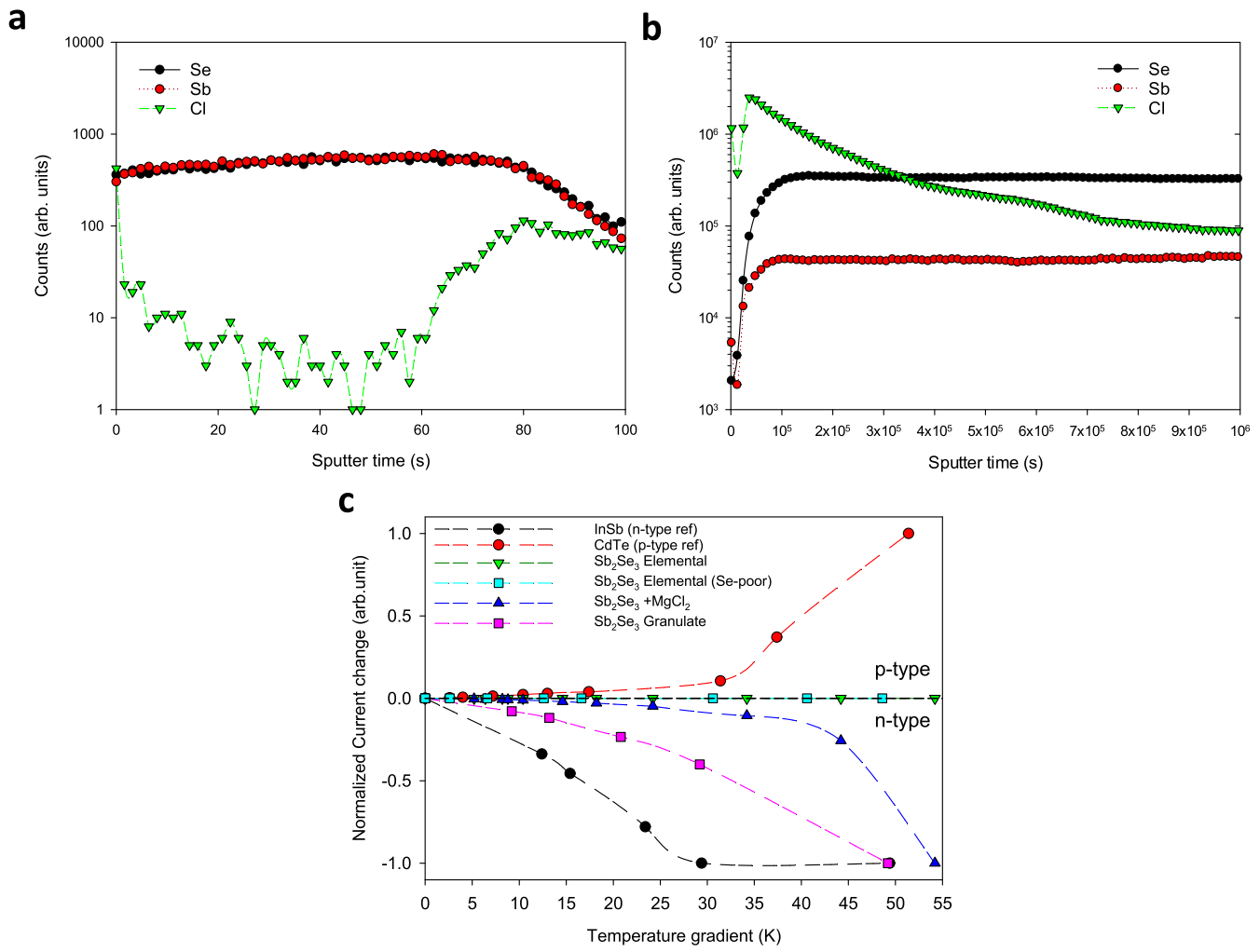

Figure 3. (a) SIMS of the Sb_2Se_3 cell structure, (b) SIMS analysis of a crystal grown from the Sb_2Se_3 source material, and (c) hot-probe comparison of the carrier-type in Sb_2Se_3 crystal grown from Sb and Se elemental precursor materials, with addition of $MgCl_2$, under Se-poor conditions and comparison with growth from the Sb_2Se_3 granulate precursor.

analysis also indicates upward band bending at the back surface, with the material being more highly n-type away from the back surface. This corresponds to the presence of a surface electron depletion layer, which may be modeled by solving the Poisson equation.[38] HAXPES analysis of the CSS-deposited thin-film material showed good agreement with the cleaved single crystal. In both cases, the material was found to be n-type and with the VBM to Fermi level position being near-identical, 0.98 eV for bulk crystals and 0.96 eV for CSS films, with the bandgap being 1.18 eV.

Recent density functional theory work on native defect formation energies by Savory et al.[18] identified that Sb_2Se_3 should be natively insulating due to the midgap pinning influence of vacancy defects. Based on this analysis and the comparatively high doping levels observed in our material, it seemed likely that our material contained unintended n-type extrinsic dopants. Clearly, impurities can arise at various points in the sample preparation. However, as both thin-film and single-crystal samples displayed similar n-type doping, but no common fabrication steps, it was suspected that contamination arose from the granulate Sb_2Se_3 source material (5 N purity Alfa Aesar), which was common to both thin films and crystals.

TOF-SIMS analysis was initially performed on a complete cell structure, as a screening process to identify possible contaminates. A number of expected contaminants were observable in the soda-lime glass layer (e.g., Na, Mg, Ce), but the only contaminant observed in all samples at significant levels within the Sb_2Se_3 layer was Cl. Figure 3a shows SIMS profiles for Sb, Se, and Cl in a TiO_2/Sb_2Se_3 CSS-deposited device (a similar Cl content was found for other CSS and thermally evaporated Sb_2Se_3 device structures, Figure S1). The Cl signal appears lower toward the free back surface (0 s sputter time), but there is accumulation primarily in the region near the Sb_2Se_3/TiO_2 interface (60−80 s sputter time). The presence of chlorine could not be otherwise accounted for and was identified as a potential n-type dopant via substitution on a Se-site. Quadrupole SIMS analysis of the single-crystal material, Figure 3b, demonstrated an even higher Cl content in the bulk crystal material. It was therefore strongly suspected that Cl contamination of the Sb_2Se_3 feedstock was the cause of n-type doping. The Sb_2Se_3 feedstock was able to be pinpointed as the source of Cl contamination as crystals and thin films shared no common fabrication steps. The only commonality between the two sample types was the source material.

Verification of Cl as the active dopant was done in two parts. First, bulk crystals were fabricated from high-purity metallic Sb and Se source materials, rather than from the Sb_2Se_3 granulate (i.e., with the removal of extrinsic impurities in the granulate

https://dx.doi.org/10.1021/acs.chemmater.0c00223
Chem. Mater. 2020, 32, 2621−2630

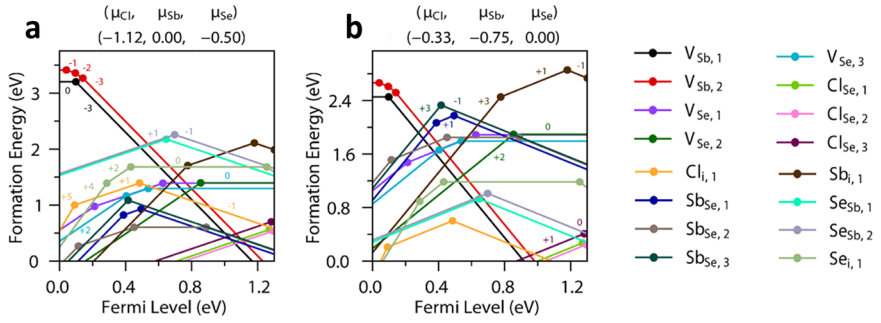

Figure 4. Defect transition-level diagrams for Sb_2Se_3 doped with Cl under limiting chemical potential conditions (A) Sb-rich and (B) Se-rich, plotting defect formation energy (eV) against the position of the Fermi level above the valence band maximum. Defect labels are given in the legend, charge states are given by the labels adjacent to the lines (with parallel lines sharing the same charge state), and transition levels are represented by filled circles.

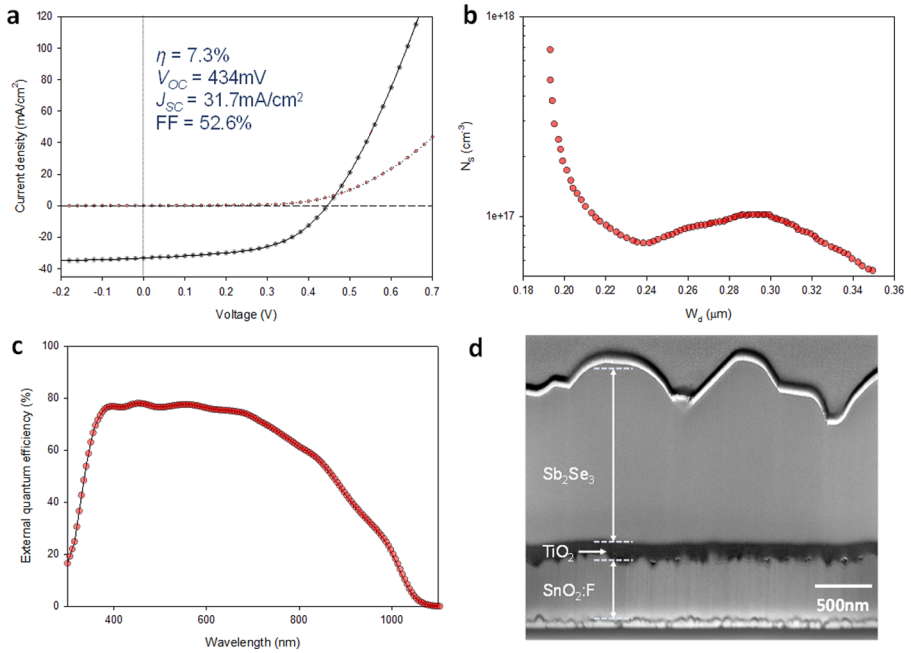

Figure 5. (a) $J-V$ curve for TiO_2/Sb_2Se_3 isotype junction, (b) shallow doping density versus depletion width calculated from capacitance voltage measurement, (c) external quantum efficiency curve, (d) SEM cross section of the device structure.

source material). These high-purity samples were found to be highly insulating, with no measurable carrier-type even by the hot probe, as shown in Figure 3c. Second, to definitively establish the role of Cl, the insulating material was reground into powder and mixed with $MgCl_2$ (0.1 atom %), a convenient Cl source used for CdTe cell processing,[14] before being recrystallized. $MgCl_2$ was additionally selected as, if active, Mg would be a p-type dopant via Mg_{Sb}, so Mg could be discounted as a source of any n-type doping observed. X-ray diffraction (XRD), Figure S3, showed no evidence of structural change or secondary phases as a result of Cl incorporation. Regardless of the formation of secondary phases, such $SbCl_3$ is not a concern given its low melting point and the fabrication temperatures used. Hot-probe analysis of the resultant crystal showed that addition of Cl converted the insulating material to n-type (Figure 3c). This is a clear demonstration that (i) on the basis of native defects, Sb_2Se_3 is insulating and (ii) Cl is an effective n-type dopant, with $MgCl_2$ being a suitable chlorine source for doping. Further to this, we also produced crystals grown from Sb and Se elemental precursors but with a Se deficiency, i.e., Se-poor conditions. This was done to rule out the possibility of selenium vacancies acting as an n-type dopant as has previously been suggested.[39] As shown in Figure 3c, Se-poor conditions produced no shift from insulating behavior and there was no indication that the n-type character resulted from native defects.

DFT calculations were then performed to examine the potential of Cl in Sb_2Se_3 as a dopant. Chlorine was introduced as a substitution on all three symmetry-inequivalent Se sites, as well as an interstitial into a 1 × 3 × 1 (60 atom) supercell, which was used in the previous ab initio study on the intrinsic defects of the Sb_2Se_3 system.[18] As such, the defect formation energies are directly comparable to the intrinsic calculations. Figure 4 depicts the transition-level diagrams under the two relevant chemical potential limits of Sb_2Se_3—(a) Sb-rich, Se-poor and (b) Se-rich, Sb-poor. $SbCl_3$ was the most stable Sb–Cl phase at $\mu(Sb) = 0$, and so its formation energy was used for the chemical potential of Cl in the Sb-rich limit, while the $P\bar{4}3n$ phase of $SeCl_4$ was the limiting Cl-containing phase in the Se-rich limit. In both chemical potential limits, Cl_{Se} is a dominant defect, with low formation energies (<0.5 eV) on all three Se sites. The Se^2 position at the edge of the Sb–Se one-

https://dx.doi.org/10.1021/acs.chemmater.0c00223
Chem. Mater. 2020, 32, 2621−2630

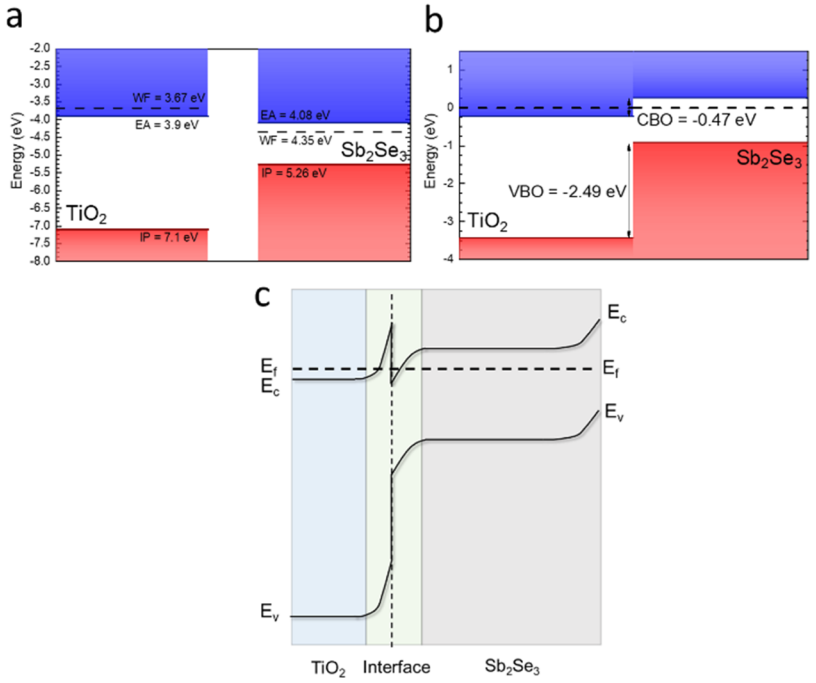

Figure 6. (a) TiO_2 and Sb_2Se_3 energy level positions determined from XPS analysis showing electron affinity (EA), work function (WF), and ionization potential (IP) of each material, (b) band alignment of the TiO_2/Sb_2Se_3 interface, and (c) proposed band structure of TiO_2/Sb_2Se_3.

dimensional (1D) ribbons is the most favorable to substitute; in all cases, this defect is likely to act as a shallow donor, with the +1/0 transition level always occurring within 25 meV of the conduction band edge. The Cl interstitial shows amphoteric behavior, similar to both Sb_i and Se_i—the interstitial region of Sb_2Se_3 allows stable situations for both Cl acting in negative and positive oxidation states—although the −1 charge state dominates for most Fermi level positions.

The primary effect of Cl doping will be to significantly shift the Fermi level position and modify Sb_2Se_3 from intrinsic to n-type. In both chemical potential conditions, Cl_{Se} will be compensated by V_{Sb} below the conduction band edge, however, moving E_F from midgap in the intrinsic regime to within 0.3 eV of the conduction band edge. This will lead to significantly higher electron concentrations. We can quantify this effect using the SC-Fermi package,[40] which self-consistently solves for the Fermi energy given a set of defect formation energies assuming thermodynamic equilibrium and overall charge neutrality. Considering the intrinsic defects alone,[18] the calculated Fermi levels lie almost exactly at the midgap: 0.632 eV above the VBM for Sb-rich and 0.641 eV for Se-rich. With the Cl defects included, the Fermi level shifts to 1.057 eV in the Sb-rich regime, only ∼0.23 eV below the HSE06 + D3 conduction band position and aligning extremely well with the observed experimental conduction band/work function separation. The predicted concentration of electrons from a Fermi−Dirac distribution at 300 K is only 6.3×10^{14} cm^{-3}, significantly greater than that from the intrinsic defects alone, but far from that observed experimentally. Furthermore, in the Se-rich regime, the Fermi level is shifted to 0.944 eV, and the predicted electron concentration is 7.9×10^{12} cm^{-3}. This model, however, assumes that the defect concentrations are at their equilibrium concentrations at 300 K, whereas the synthesis of the material occurs at a much higher temperature. At elevated temperatures, defects will be more prevalent and some of these may be retained in the films. To model this situation, SC-Fermi can calculate the self-consistent Fermi level at 300 K, but where the defects are fixed at their concentrations for fabrication temperatures of 700 K. For both chemical potential regimes, this shifts the Fermi level to ∼1.27 eV and increases the predicted electron concentration to 2.5×10^{18} cm^{-3} (Se-rich) or to 2.1×10^{20} cm^{-3} (Sb-rich). In reality, the defect concentrations in the synthesized samples will lie somewhere between these two extremes, in line with the 10^{16}–10^{17} cm^{-3} electron concentration observed experimentally.

Complete solar cell structures were fabricated from the granulate source material established to be n-type doped due to the presence of Cl. Figure 5a shows $J-V$ data for a TiO_2/Sb_2Se_3 device with associated $C-V$ data converted into shallow doping (N_s) versus depletion width (W_d) in Figure 5b and EQE in Figure 5c. Compared to cell structures reported in our prior work,[2,15] the efficiency has been increased by the inclusion of a sputtered TiO_2 layer, prior to solution deposition of a thicker TiO_2 film. This creates uniform TiO_2 coverage, as seen from the cross-sectional scanning electron microscopy (SEM) image in Figure 5d, reducing shunting losses occurring due to the TiO_2 layer and thus improving the fill factor (FF). This structure has so far yielded a peak PCE of 7.3% with V_{OC} = 434 mV, J_{SC} = 31.7 mA/cm^2, and FF = 52.6%. From the analysis of capacitance voltage measurements (Figure 5b), the apparent doping density, now established to be donor doping, was ∼10^{17} cm^{-3}. The increase to >10^{17} cm^{-3} at W_d < 0.2 μm is due to the influence of the back contact, as commonly observed for CdTe solar cells,[41] rather than a genuine increase in doping.

Critically, given our identification of the absorber as n-type, the device clearly does not have the standard p−n junction architecture, and as such our TiO_2/Sb_2Se_3 device is better described as an n−n isotype heterojunction.[42,43] An important point of note is to recognize that $J-V$ and $C-V$ analyses of a device junction in isolation cannot determine the majority carrier-type of the absorber. $C-V$ measures the capacitance

https://dx.doi.org/10.1021/acs.chemmater.0c00223
Chem. Mater. 2020, 32, 2621−2630

change of the depletion region extending with applied bias, from which the carrier density, but not type, of the absorber may be inferred. For thin-film PV devices, including Sb_2Se_3 ones, it is a common assumption that they operate as a one-sided p−n junction and $C-V$ data is then interpreted using the appropriate $C-V$ relation. However, the p and n designations simply relate to the Fermi level position relative to the midgap. The direction of carrier flow is essentially independent of such classifications and is determined by the relative Fermi level positions of the two partner layers, as well as the conduction and valence band offsets. If carrier flow under illumination is in the same direction, an n−n, or indeed p−p, isotype junction is essentially indistinguishable from a p−n junction by the $J-V$ and $C-V$ behavior alone.[42]

To assess the functionality of our device structure, band positions were determined for device layers via XPS. Figure 6a shows work function, electron affinity (EA), and ionization potential (IP) values determined for Sb_2Se_3 and TiO_2 thin films via XPS analysis (raw data is given in Figure S2, Supporting Information). The "natural" band alignment of the two layers based on VBM, conduction band minimum (CBM), and Fermi level positions is shown in Figure 6b with a proposed band diagram for the resultant structure in Figure 6c. The TiO_2 layer was measured with a degenerate Fermi level position, indicative of a significant downward band bending at the surface.[44] The bulk of the TiO_2 film will likely have nondegenerate doping; however, this surface Fermi level position is considered more representative for junction formation. When the Sb_2Se_3 and TiO_2 layers are brought into contact, electrons flow from the material with the higher Fermi level (TiO_2: −3.67 eV) to the lower Fermi level (Sb_2Se_3: −4.35 eV), creating a built-in potential V_{bi} in the same direction as would be anticipated for a p−n junction. A spike and trough occur in the near-interface region due to the charge transfer. The respective conduction and valence band offsets also favor electron extraction through the TiO_2. Compared to an equivalent p−n junction architecture, the built-in voltage will be reduced but this has essentially been traded off for the benefit of higher carrier concentration. This demonstration of Sb_2Se_3 solar cells being based on an n−n isotype junction begs a number of questions; (i) which carrier-type is truly optimal for the performance of such solar cells?, (ii) can device designs be improved on the basis of an n-type absorber?, (iii) are p-type doping processes required, and (iv) can p−n, or indeed p−i−n/n−i−p, junction structures be fabricated by controlled doping approaches? Finally, we would emphasize that our results do not imply that all reported Sb_2Se_3 solar cells, from varied deposition processes and source materials, are n-type. The Cl contamination, and thus n-type doping, appears results from a synthesis step of the Sb_2Se_3 granulate material. As this is an industrial process that we do not have access to, it is difficult to identify the specific source. It is also not possible to say whether this is a common contaminant that will be present in the Sb_2Se_3 material purchased from all manufacturers. Rather, we would suggest researchers working on such devices be advised to carefully determine the carrier-type of the material being used, rather than assuming the p-type character. We have however demonstrated a route for Sb_2Se_3 synthesis from metallic precursors by which the doping can be more consistently controlled. This work clearly shows how the presence of extrinsic impurities can have a profound and unexpected effect on the material and on devices built from it.

CONCLUSIONS

In this work, we have demonstrated that Sb_2Se_3 can be utilized as an n-type absorber layer to produce isotype thin-film solar cells. This was shown via a range of complementary analyses on both a thin-film solar cell and bulk crystal material. The source of the n-type doping in devices was identified to be Cl impurities in the Sb_2Se_3 source material, leading to n-type carrier concentrations in the range of 10^{16}−10^{17} cm^{-3}. This was verified through the fabrication of insulating bulk crystals from pure metallic (i.e., Cl-free) precursors, which were subsequently doped n-type via addition of Cl from $MgCl_2$. DFT calculations of associated Cl defect levels showed the Cl substitutional on the Se sites to be a shallow donor level with low formation energy, although the Cl_i defect could introduce a potential deep level compensating defect.

ASSOCIATED CONTENT

Supporting Information

The Supporting Information is available free of charge at https://pubs.acs.org/doi/10.1021/acs.chemmater.0c00223.

Secondary ion mass spectrometry of different thin-film Sb_2Se_3 devices, secondary electron cutoff and valence band maxima obtained from X-ray photoelectron spectroscopy analysis of TiO_2 and Sb_2Se_3 thin films, and X-ray diffraction data of Sb_2Se_3 crystals with and without the addition of Cl (PDF)

AUTHOR INFORMATION

Corresponding Author

Jonathan D. Major − *Department of Physics, Stephenson Institute for Renewable Energy, University of Liverpool, Liverpool L69 7ZF, U.K.;* orcid.org/0000-0002-5554-1985; Email: jon.major@liverpool.ac.uk

Authors

Theodore D. C. Hobson − *Department of Physics, Stephenson Institute for Renewable Energy, University of Liverpool, Liverpool L69 7ZF, U.K.;* orcid.org/0000-0002-0013-360X

Laurie J. Phillips − *Department of Physics, Stephenson Institute for Renewable Energy, University of Liverpool, Liverpool L69 7ZF, U.K.*

Oliver S. Hutter − *Department of Physics, Stephenson Institute for Renewable Energy, University of Liverpool, Liverpool L69 7ZF, U.K.*

Huw Shiel − *Department of Physics, Stephenson Institute for Renewable Energy, University of Liverpool, Liverpool L69 7ZF, U.K.*

Jack E. N. Swallow − *Department of Physics, Stephenson Institute for Renewable Energy, University of Liverpool, Liverpool L69 7ZF, U.K.*

Christopher N. Savory − *Department of Chemistry, Kathleen Lonsdale Materials Chemistry and Thomas Young Centre, University College London, London WC1H 0AJ, U.K.;* orcid.org/0000-0002-9052-7484

Pabitra K. Nayak − *Clarendon Laboratory, Department of Physics, University of Oxford, Oxford OX1 3PU, U.K.; TIFR Centre for Interdisciplinary Sciences, Tata Institute of Fundamental Research, Hyderabad 500107, India*

Silvia Mariotti − *Department of Physics, Stephenson Institute for Renewable Energy, University of Liverpool, Liverpool L69 7ZF,*

U.K.
Bhaskar Das − *Department of Chemical Engineering and Materials Science, University of Minnesota, Minneapolis, Minnesota 55455-0132, United States*
Leon Bowen − *G. J. Russell Microscopy Facility, Department of Physics, University of Durham, Durham DH1 3LE, U.K.*
Leanne A. H. Jones − *Department of Physics, Stephenson Institute for Renewable Energy, University of Liverpool, Liverpool L69 7ZF, U.K.*
Thomas J. Featherstone − *Department of Physics, Stephenson Institute for Renewable Energy, University of Liverpool, Liverpool L69 7ZF, U.K.*
Matthew J. Smiles − *Department of Physics, Stephenson Institute for Renewable Energy, University of Liverpool, Liverpool L69 7ZF, U.K.*
Mark A. Farnworth − *NSG-Pilkington, Lancashire L40 5UF, U.K.*
Guillaume Zoppi − *Department of Mathematics, Physics & Electrical Engineering, Northumbria University, Newcastle upon Tyne NE1 8ST, U.K.;* orcid.org/0000-0003-3622-6899
Pardeep K. Thakur − *Diamond Light Source Ltd., Oxfordshire OX11 0DE, U.K.;* orcid.org/0000-0002-9599-0531
Tien-Lin Lee − *Diamond Light Source Ltd., Oxfordshire OX11 0DE, U.K.*
Henry J. Snaith − *Clarendon Laboratory, Department of Physics, University of Oxford, Oxford OX1 3PU, U.K.;* orcid.org/0000-0001-8511-790X
Chris Leighton − *Department of Chemical Engineering and Materials Science, University of Minnesota, Minneapolis, Minnesota 55455-0132, United States;* orcid.org/0000-0003-2492-0816
David O. Scanlon − *Department of Chemistry, Kathleen Lonsdale Materials Chemistry and Thomas Young Centre, University College London, London WC1H 0AJ, U.K.; Diamond Light Source Ltd., Oxfordshire OX11 0DE, U.K.;* orcid.org/0000-0001-9174-8601
Vinod R. Dhanak − *Department of Physics, Stephenson Institute for Renewable Energy, University of Liverpool, Liverpool L69 7ZF, U.K.*
Ken Durose − *Department of Physics, Stephenson Institute for Renewable Energy, University of Liverpool, Liverpool L69 7ZF, U.K.*
Tim D. Veal − *Department of Physics, Stephenson Institute for Renewable Energy, University of Liverpool, Liverpool L69 7ZF, U.K.*

Complete contact information is available at: https://pubs.acs.org/10.1021/acs.chemmater.0c00223

Author Contributions

T.D.C.H. prepared and characterized bulk crystal samples under the guidance of K.D. L.J.P. and O.S.H. prepared thin films and solar cells with assistance from J.D.M. J.E.N.S., H.S., L.A.H.J., T.J.F., and M.J.S. performed photoelectron spectroscopy measurements and analysis with assistance from P.K.T. and T.-L.L. and input from T.D.V. and V.R.D. C.N.S. and D.O.S. performed DFT calculations. Hall measurements were carried out by B.D., supervised by C.L. P.K.N. and S.M. performed SVM measurements with input from H.J.S. Cross-sectional cell images were produced by L.B., SIMS analysis by G.Z. and M.A.F. J.D.M. coordinated the project and prepared the manuscript, with input from all authors.

Funding

Funding for the work was provided by EPSRC via EP/N014057/1, EP/L01551X/1, EP/P02484X/1, and EP/R513271/1. We acknowledge Diamond Light Source for time on Beamline I09 under Proposal No. SI21431-1. The uses of the UCL Legion, Myriad, and Grace High Performance Computing Facilities (Legion@UCL, Myriad@UCL, and Grace@UCL) are acknowledged in the production of this work. Computational work was also performed on the ARCHER UK National Supercomputing Service, via our membership of the UK's HEC Materials Chemistry Consortium, funded by EPSRC (EP/L000202). Work at the University of Minnesota was supported by the customers of Xcel Energy through a grant from the renewable development fund. Data files related to the project are available from http://datacat.liverpool.ac.uk/id/eprint/1029 or from the corresponding author.

Notes

The authors declare no competing financial interest.

REFERENCES

(1) Birkett, M.; Linhart, W. M.; Stoner, J.; Phillips, L. J.; Durose, K.; Alaria, J.; Major, J. D.; Kudrawiec, R.; Veal, T. D. Band Gap Temperature-Dependence of Close-Space Sublimation Grown Sb2Se3 by Photo-Reflectance. *APL Mater.* **2018**, *6*, No. 084901.
(2) Phillips, L. J.; Savory, C. N.; Hutter, O. S.; Yates, P. J.; Shiel, H.; Mariotti, S.; Bowen, L.; Birkett, M.; Durose, K.; Scanlon, D. O.; Major, J. D. Current Enhancement via a TiO2 Window Layer for CSS Sb2Se3 Solar Cells: Performance Limits and High V_{Oc}. *IEEE J. Photovoltaics* **2019**, *9*, 544−551.
(3) Zhou, Y.; Wang, L.; Chen, S.; Qin, S.; Liu, X.; Chen, J.; Xue, D.-J.; Luo, M.; Cao, Y.; Cheng, Y.; Sargent, E. H.; Tang, J. Thin-Film Sb2Se3 Photovoltaics with Oriented One-Dimensional Ribbons and Benign Grain Boundaries. *Nat. Photonics* **2015**, *9*, 409−415.
(4) Messina, S.; Nair, M. T. S.; Nair, P. K. Antimony Selenide Absorber Thin Films in All-Chemically Deposited Solar Cells. *J. Electrochem. Soc.* **2009**, *156*, No. H327.
(5) Liu, X.; Chen, J.; Luo, M.; Leng, M.; Xia, Z.; Zhou, Y.; Qin, S.; Xue, D.-J.; Lv, L.; Huang, H.; Niu, D.; Tang, J. Thermal Evaporation and Characterization of Sb2Se3 Thin Film for Substrate Sb2Se3/CdS Solar Cells. *ACS Appl. Mater. Interfaces* **2014**, *6*, 10687−10695.
(6) Zhou, Y.; Leng, M.; Xia, Z.; Zhong, J.; Song, H.; Liu, X.; Yang, B. Solution-Processed Antimony Selenide Heterojunction Solar Cells. *Adv. Energy Mater.* **2014**, No. 1301846.
(7) Chen, C.; Wang, L.; Gao, L.; Nam, D.; Li, D.; Li, K.; Zhao, Y.; Ge, C.; Cheong, H.; Liu, H.; Song, H.; Tang, J. 6.5% Certified Efficiency Sb_2Se_3 Solar Cells Using PbS Colloidal Quantum Dot Film as Hole-Transporting Layer. *ACS Energy Lett.* **2017**, *2*, 2125−2132.
(8) Wen, X.; Chen, C.; Lu, S.; Li, K.; Kondrotas, R.; Zhao, Y.; Chen, W.; Gao, L.; Wang, C.; Zhang, J.; Niu, G.; Tang, J. Vapor Transport Deposition of Antimony Selenide Thin Film Solar Cells with 7.6% Efficiency. *Nat. Commun.* **2018**, *9*, No. 2179.
(9) Li, Z.; Liang, X.; Li, G.; Liu, H.; Zhang, H.; Guo, J.; Chen, J.; Shen, K.; San, X.; Yu, W.; Schropp, R. E. I.; Mai, Y. 9.2%-Efficient Core-Shell Structured Antimony Selenide Nanorod Array Solar Cells. *Nat. Commun.* **2019**, *10*, No. 125.
(10) Wong, L. H.; Zakutayev, A.; Major, J. D.; Hao, X.; Walsh, A.; Todorov, T. K.; Saucedo, E. Emerging Inorganic Solar Cell Efficiency Tables (Version 1). *J. Phys. Energy* **2019**, *1*, No. 032001.
(11) Spalatu, N.; Hiie, J.; Kaupmees, R.; Volobujeva, O.; Krustok, J.; Acik, I. O.; Krunks, M. Postdeposition Processing of SnS Thin Films and Solar Cells: Prospective Strategy to Obtain Large, Sintered, and Doped SnS Grains by Recrystallization in the Presence of a Metal Halide Flux. *ACS Appl. Mater. Interfaces* **2019**, *11*, 17539−17554.
(12) Major, J. D.; Durose, K. Early Stage Growth Mechanisms of CdTe Thin Films Deposited by Close Space Sublimation for Solar Cells. *Sol. Energy Mater. Sol. Cells* **2011**, *95*, 3165−3170.

(13) Major, J. D.; Proskuryakov, Y. Y.; Durose, K.; Zoppi, G.; Forbes, I. Control of Grain Size in Sublimation-Grown CdTe, and the Improvement in Performance of Devices with Systematically Increased Grain Size. *Sol. Energy Mater. Sol. Cells* **2010**, *94*, 1107−1112.
(14) Major, J. D.; Treharne, R. E.; Phillips, L. J.; Durose, K. A Low-Cost Non-Toxic Post-Growth Activation Step for CdTe Solar Cells. *Nature* **2014**, *511*, 334.
(15) Hutter, O. S.; Phillips, L. J.; Durose, K.; Major, J. D. 6.6% Efficient Antimony Selenide Solar Cells Using Grain Structure Control and an Organic Contact Layer. *Sol. Energy Mater. Sol. Cells* **2018**, *188*, 177−181.
(16) Whittaker-Brooks, L.; Gao, J.; Hailey, A. K.; Thomas, C. R.; Yao, N.; Loo, Y.-L. Bi_2S_3 Nanowire Networks as Electron Acceptor Layers in Solution-Processed Hybrid Solar Cells. *J. Mater. Chem. C* **2015**, *3*, 2686−2692.
(17) Bacewicz, R.; Ciszek, T. F. Liquid Encapsulated Crystal Growth and Electrical Properties of Sb_2Se_3 and Bi2S3. *J. Cryst. Growth* **1991**, *109*, 133−136.
(18) Savory, C. N.; Scanlon, D. O. The Complex Defect Chemistry of Antimony Selenide. *J. Mater. Chem. A* **2019**, 10739−10744.
(19) Zhou, Y.; Leng, M.; Xia, Z.; Zhong, J.; Song, H.; Liu, X.; Yang, B.; Zhang, J.; Chen, J.; Zhou, K.; Han, J.; Cheng, Y.; Tang, J. Solution-Processed Antimony Selenide Heterojunction Solar Cells. *Adv. Energy Mater.* **2014**, *4*, No. 1301846.
(20) Zhou, Y.; Li, Y.; Luo, J.; Li, D.; Liu, X.; Chen, C.; Song, H.; Ma, J.; Xue, D.-J.; Yang, B.; Tang, J. Buried Homojunction in CdS/Sb_2Se_3 Thin Film Photovoltaics Generated by Interfacial Diffusion. *Appl. Phys. Lett.* **2017**, *111*, No. 013901.
(21) Li, K.; Wang, S.; Chen, C.; Kondrotas, R.; Hu, M.; Lu, S.; Wang, C.; Chen, W.; Tang, J. 7.5% n−i−p Sb_2Se_3 Solar Cells with CuSCN as a Hole-Transport Layer. *J. Mater. Chem. A* **2019**, *7*, 9665−9672.
(22) Ghosh, G. The Sb-Se (Antimony-Selenium) System. *J. Phase Equilibria* **1993**, *14*, 753−763.
(23) Hobson, T. D. C.; Hutter, O. S.; Birkett, M.; Veal, T. D.; Durose, K. In *Growth and Characterization of Sb_2Se_3 Single Crystals for Fundamental Studies*, IEEE Photovoltaic Specialists Conferences, Hawaii, 2018; pp 3−7.
(24) van der Pauw, L. J. A Method of Measuring the Resistivity and Hall Coefficient on Lamellae of Arbitrary Shape. *Phillips Tech. Rev.* **1958**, *20*, 220.
(25) Kresse, G.; Hafner, J. *Ab Initio* Molecular Dynamics for Liquid Metals. *Phys. Rev. B* **1993**, *47*, 558−561.
(26) Kresse, G.; Hafner, J. *Ab Initio* Molecular-Dynamics Simulation of the Liquid-Metal−Amorphous-Semiconductor Transition in Germanium. *Phys. Rev. B* **1994**, *49*, 14251−14269.
(27) Kresse, G.; Furthmüller, J. Efficient Iterative Schemes for *Ab Initio* Total-Energy Calculations Using a Plane-Wave Basis Set. *Phys. Rev. B* **1996**, *54*, 11169−11186.
(28) Kresse, G.; Furthmüller, J. Efficiency of Ab-Initio Total Energy Calculations for Metals and Semiconductors Using a Plane-Wave Basis Set. *Comput. Mater. Sci.* **1996**, *6*, 15−50.
(29) Krukau, A. V.; Vydrov, O. A.; Izmaylov, A. F.; Scuseria, G. E. Influence of the Exchange Screening Parameter on the Performance of Screened Hybrid Functionals. *J. Chem. Phys.* **2006**, *125*, No. 224106.
(30) Grimme, S. Accurate Description of van Der Waals Complexes by Density Functional Theory Including Empirical Corrections. *J. Comput. Chem.* **2004**, *25*, 1463−1473.
(31) Freysoldt, C.; Neugebauer, J.; Van de Walle, C. G. Fully *Ab Initio* Finite-Size Corrections for Charged-Defect Supercell Calculations. *Phys. Rev. Lett.* **2009**, *102*, No. 016402.
(32) Lany, S.; Zunger, A. Assessment of Correction Methods for the Band-Gap Problem and for Finite-Size Effects in Supercell Defect Calculations: Case Studies for ZnO and GaAs. *Phys. Rev. B* **2008**, *78*, No. 235104.
(33) Murphy, S. T.; Hine, N. D. M. Anisotropic Charge Screening and Supercell Size Convergence of Defect Formation Energies. *Phys. Rev. B* **2013**, *87*, No. 094111.
(34) Golan, G.; Axelevitch, A.; Gorenstein, B.; Manevych, V. Hot-Probe Method for Evaluation of Impurities Concentration in Semiconductors. *Microelectron. J.* **2006**, *37*, 910−915.
(35) Walter, J.; Zhang, X.; Voigt, B.; Hool, R.; Manno, M.; Mork, F.; Aydil, E. S.; Leighton, C. Surface Conduction in n-Type Pyrite FeS_2 Single Crystals. *Phys. Rev. Mater.* **2017**, *1*, No. 065403.
(36) Chen, C.; Bobela, D. C.; Yang, Y.; Lu, S.; Zeng, K.; Ge, C.; Yang, B.; Gao, L.; Zhao, Y.; Beard, M. C.; Tang, J. Characterization of Basic Physical Properties of Sb2Se3 and Its Relevance for Photovoltaics. *Front. Optoelectron.* **2017**, *10*, 18−30.
(37) Shiel, H.; Hutter, O.; Phillips, L.; Al Turkestani, M.; Dhanak, V. R.; Veal, T. D.; Durose, K.; Major, J. D. Chemical Etching of Sb2Se3 Solar Cells: Surface Chemistry and Back Contact Behaviour. *J. Phys. Energy* **2019**, *1*, No. 045001.
(38) Veal, T. D.; Piper, L. F. J.; Schaff, W. J.; McConville, C. F. Inversion and Accumulation Layers at InN Surfaces. *J. Cryst. Growth* **2006**, *288*, 268−272.
(39) Liu, X.; Xiao, X.; Yang, Y.; Xue, D.-J.; Li, D.-B.; Chen, C.; Lu, S.; Gao, L.; He, Y.; Beard, M. C.; Wang, G.; Chen, S.; Tang, J. Enhanced Sb_2Se_3 Solar Cell Performance through Theory-Guided Defect Control. *Prog. Photovoltaics* **2017**, *25*, 861−870.
(40) Buckeridge, J. Equilibrium Point Defect and Charge Carrier Concentrations in a Material Determined through Calculation of the Self-Consistent Fermi Energy. *Comput. Phys. Commun.* **2019**, *244*, 329−342.
(41) Li, J. V.; Halverson, A. F.; Sulima, O. V.; Bansal, S.; Burst, J. M.; Barnes, T. M.; Gessert, T. A.; Levi, D. H. Theoretical Analysis of Effects of Deep Level, Back Contact, and Absorber Thickness on Capacitance-Voltage Profiling of CdTe Thin-Film Solar Cells. *Sol. Energy Mater. Sol. Cells* **2012**, *100*, 126−131.
(42) Sharma, B. L.; Purohit, R. K. *Semiconductor Heterojunctions*, 1st ed.; Pergamon Press: Oxford, 1974.
(43) Chuang, S. L. *Physics of Optoelectronic Devices*; Wiley: New York, 1995.
(44) Ozawa, K.; Emori, M.; Yamamoto, S.; Yukawa, R.; Yamamoto, S.; Hobara, R.; Fujikawa, K.; Sakama, H.; Matsuda, I. Electron-Hole Recombination Time at TiO2 Single-Crystal Surfaces: Influence of Surface Band Bending. *J. Phys. Chem. Lett.* **2014**, *5*, 1953−1957.

https://dx.doi.org/10.1021/acs.chemmater.0c00223
Chem. Mater. 2020, 32, 2621−2630